Selective laser melting of Hastelloy X nanocomposite: effects of TiC reinforcement on crack elimination and strength improvement

Quanquan Han[a,b,c*], Yuchen Gu[d*], Jun Huang[a,b], Liqiao Wang [e*], Kenny W. Q. Low[d], Qixiang Feng[f], Yingyue Yin[a,b*], Rossitza Setchi[c]

[a]Key Laboratory of High Efficiency and Clean Mechanical Manufacture of Ministry of Education, Center for Additive Manufacturing, School of Mechanical Engineering, Shandong University, Jinan, 250061, China

[b]Key National Demonstration Center for Experimental Mechanical Engineering Education, Shandong University, Jinan, 250061, China

[c]Cardiff School of Engineering, Cardiff University, Cardiff, CF24 3AA, UK

[d]College of Engineering, Swansea University, Swansea, SA1 8EN, UK

[e]Cardiff Business School, Cardiff University, Cardiff, CF10 3EU, UK

[f]College of Mechanical Engineering, Chongqing University, Chongqing, 40044, China

Corresponding authors:

Quanquan Han: Hanquanquan@sdu.edu.cn, +4402920876266

Yuchen Gu: yuchen.gu@swansea.ac.uk, +4407859204503

Liqiao Wang: Wangl45@cardiff.ac.uk, +4407729282402

Yingyue Yin: yinyingyue1999@163.com, +860531-88392608

Abstract

The Hastelloy X (HX) nickel-based superalloy is increasingly applied in the aerospace industry because of its exceptional combination of oxidation resistance and high-temperature strength. The addition of nanoscale ceramic reinforcements to the HX alloy is expected to further improve its mechanical and thermophysical performance. The research challenge is to manufacture HX nanocomposites using additive manufacturing (AM) technologies, particularly selective laser melting (SLM), which has been used successfully to produce other nanocomposites. This paper systematically studies the microstructure and tensile performance of HX-3 wt.% TiC nanocomposite fabricated via SLM and explores the effects of TiC nanoparticles on hot-cracking elimination and strength enhancement. The findings reveal that the addition of 3 wt.% TiC nanoparticles resulted in (1) an extra 73 J/mm^3 laser-energy density needed to manufacture nearly full-density nanocomposite samples and (2) intergranular microcrack elimination due to the significant increase in grain boundaries induced by the grain refinement. The results showed a 17% increase in yield strength, while the elongation to failure was not significantly reduced. The results from the microstructure

examination suggest that the strengthening mechanisms of load bearing and enhanced-dislocation density were the most pronounced mechanisms in the SLM-fabricated nanocomposite. These findings offer a promising pathway to strengthen mechanical performance by addressing the hot-cracking issue in the AM of nickel-based superalloys that suffer from cracking susceptibility. The results can also help to accelerate the uptake of AM in high-performance and defect-free superalloys for various applications.

1. Introduction

Selective laser melting (SLM) is an additive manufacturing (AM) technology based on laser powder beds in which a high-power laser is used to manufacture advanced metallic components with very complex geometries [1][2][3]. One of the advantages of SLM is its ability to reduce production costs and lead times, especially for high-performance parts that are required in limited quantities [4]. The SLM technology has been successfully employed to fabricate various high-performance metallic materials, including titanium [5][6], aluminum [7], nickel-based superalloys and their composites [8][9]. In addition, various post treatments have been used to achieve the trade-off between strength and ductility of the SLM-fabricated components. Hastelloy X (HX) is a solid-solution-strengthened, nickel-based, high-temperature alloy that is widely used in gas turbine engines, such as combustion-zone components, because of its exceptional combination of oxidation resistance, processability and high-temperature strength [10]. For these reasons, the SLM of HX alloy is thought to be a promising technology for the manufacture of the complex high-performance structural components used in gas turbine engine combustors and various petrochemical applications.

Metal matrix nanocomposites (MMNCs) are metal matrix composites (MMCs) in which the nanoparticles are employed as the reinforcement phase. Due to their nanoscale structure, MMNCs exhibit an advantage over MMCs with microscale reinforcements in terms of wear resistance, improved damping properties and mechanical strength, thus making them more attractive for various applications [11][12]. Despite the material's superior properties and the growing interest in the field,

the great potential of MMNCs has been limited, because the processing methods are expensive and difficult to scale up to manufacture large and complex shapes in bulk. The conventional methods for producing MMNCs can generally be categorised into three types: solid-state methods, semi-solid-state methods and liquid-state methods [13]. The significant disadvantages of these fabrication methods, however, include high energy consumption and difficulty in manufacturing complex-shaped components. Considering the layer-by-layer manufacturing principle of SLM, the SLM of MMNCs offers significant potential for manufacturing high-performance MMNCs with complex geometries.

In recent years, researchers have used SLM technology to manufacture various MMNCs and biocomposites [4][14]. For instance, the typically investigated nickel-based nanocomposites include TiC/Inconel 718 nanocomposites [15][16], carbon nanotube/Inconel 625 composites [17] and TiN/Inconel 718C composites [18]. The findings from these studies demonstrated that, compared to the as-fabricated matrix materials, SLM-fabricated nanocomposites exhibited higher tensile strength but lower elongation due to the ensuing grain refinement. Compared with the aforementioned nickel-based alloys, however, researchers have found HX alloy to be susceptible to hot cracking when processed using the SLM process. Previous studies have also revealed that microcracks cannot be eliminated even under optimum manufacturing conditions [19][20][21]. In one study, the hot-cracking defect was addressed by modifying the chemical composition; the reduction of Mn and Si content in that study managed to reduce the hot cracks' density so that an increase in tensile strength at elevated temperature (1,033 K) was achieved, but the microcracks still could not be eliminated [19]. Post-treatments such as hot isostatic pressing (HIP) are reportedly able to close hot cracks and improve the strength-ductility trade-off of SLM as-fabricated HX components. Although the microcracks were successfully eliminated in the HIP-processed HX components in the present study, the HIP resulted in significant degradation of tensile strength due to grain growth within the heat-treatment process. The reduction in yield strength was found to be up to 20%, although a 15% increase in elongation to failure is reportedly achievable [22][23]. The cost of extra post-processing significantly reduces the economic attractiveness of the SLM process, however, so this type of post-treatment is not an ideal alternative for mitigating hot-cracking defects. Sanchez-Mata et al. [24] studied the microstructure of SLM-

fabricated HX alloy, and while they did not detect microcracks during their optical microscopy inspection, the authors also did not detail the manufacturing conditions they used.

In one previous study by the authors, a novel method to eliminate hot-cracking defects was developed by introducing 1 wt.% TiC nanoparticles [25]. TiC nanoparticles were selected because the TiC lattice structure exhibits a smaller planar crystallographic disregistry with a nickel (Ni) lattice structure compared to other widely used nucleating agents such as SiC, Zr, ZrC and WC lattice structures. The results demonstrated that the addition of 1 wt.% TiC nanoparticles contributed to the elimination of microcracks and a 98 MPa increase in yield strength without undue sacrifices in ductility. An increase in TiC nanoparticle content could enable a further increase in tensile strength and wear performance of the fabricated HX nanocomposites, but the nanoparticles are prone to agglomeration due to the strong surface energy and poor wettability found within the molten metal matrices if the content is above the threshold. The TiC clusters may function as stress-concentration sites, thus degrading mechanical performance.

In this context, the present study examines SLM-fabricated HX nanocomposite with an addition of 3 wt.% TiC nanoparticles, with an emphasis on the effect of the TiC nanoparticles on cracking elimination and tensile-performance enhancement. The significant contribution of the current study compared to the earlier work [25] is that with an increase in TiC nanoparticle content from 1 wt.% to 3 wt.%, the primary strengthening mechanisms were found to change from grain refinement strengthening and CTE (coefficient of thermal expansion) mismatch strengthening mechanisms to load bearing strengthening and CTE mismatch strengthening mechanisms. The study also examines any defects in the as-fabricated nanocomposite caused by the added 3 wt.% nanoparticle reinforcements. Thus, this study provides practical insights into the selection of nanoscale reinforcement content in order to fabricate both high-strength and defect-free nanocomposites using SLM technology.

2. Materials and methods

2.1. Feedstock for selective laser melting

The commercial gas-atomised Hastelloy X (HX) powder used in this work was supplied from Sandvik Osprey (Neath, UK), with an alloying composition (wt.%) of 22.2Cr–19.1Fe–8.9Mo–2Co–0.13C–0.7W–0.18Si–0.17Mn–bal. Ni based on the inductively coupled plasma (ICP) analysis. The raw HX powder was measured to vary from 11.2 µm to 66.9 µm, with an average particle size of 32.5 µm based on an analysis of particle-size distribution using the Malvern Mastersizer3000 (Malvern, UK) (Fig. 1a/c). Note that the HX powder used in the present study consisted of recycled powder rather than virgin HX. An electron backscatter diffraction (EBSD) analysis of the HX powder demonstrated that very fine grains (with an average grain size of < 7 µm) formed in the powder during the gas-atomisation process, while no apparent defects such as pores or microcracks were observed (Fig. 1b). The TiC nanoparticles (< 200 nm), which functioned as a reinforcement phase in this work, were acquired from Sigma Aldrich (UK).
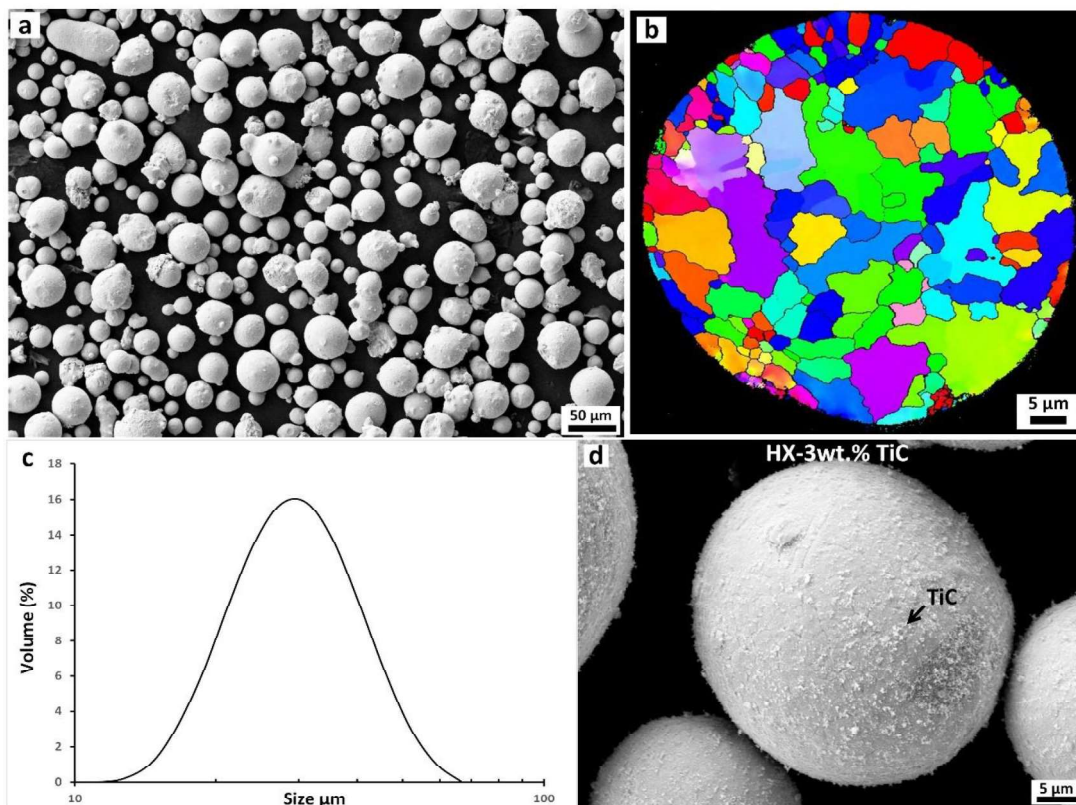

Fig. 1. The feedstock used for selective laser melting: (a) recycled Hastelloy X; (b) EBSD orientation map for HX powder; (c) particle-size distribution of HX powder; (d) mixed Hastelloy X with 3 wt.% TiC.

A commercial high-speed mixer (SpeedMixer, DAC 800.1 FVZ, Hauschild, Germany) with a maximum mixing speed of 2,000 rpm was employed to prepare the

HX-3 wt.% TiC nanocomposite feedstock. The device allows for mixing 500 g powder at once at room temperature. The mixing parameters included a 1,200 rpm mixing speed with a total of 5 min of mixing time. To prevent overheating, the mixing procedure was to mix for 2.5 min, pause for 5 min, and then mix again for 2.5 min. Fig. 1d shows the prepared nanocomposite used for SLM, in which TiC nanoparticles were uniformly distributed amongst the HX particles without settling. This uniform distribution confirmed that the high-speed mixing technique was capable of breaking up the TiC clusters and properly coating the nanoparticles to prepare the nanocomposite feedstock for SLM. It should be noted that the added 3 wt.% of TiC nanoparticles were determined to be the highest percentage achieved suitable for SLM of HX superalloy. This is because significant TiC nanoparticles agglomeration occurred in the powder feedstock when the TiC content is greater than 3 wt.%, indicating that the high-speed mixing technique could not break up the TiC clusters while the TiC nanoparticle percentage is over the threshold of 3 wt.%. The powder feedstock with TiC clusters is not considered to be suitable for SLM process, because the TiC clusters could function as stress-concentration sites and degrade the mechanical properties through the formation of pores and cracks.

2.2. Selective laser melting process

The apparatus used for the specimens manufactured in this work was a Renishaw AM250 (Renishaw Plc, UK) equipped with a modulated ytterbium fibre laser (wavelength = 1,071 nm). The SLM process starts by slicing the 3D CAD file data into layers, usually from 20 to 100 μm thick, creating a 2D image of each layer; thin layers of atomised fine metal powder are evenly distributed using a coating mechanism onto a substrate plate. This takes place inside a chamber containing a controlled atmosphere of inert gas, either argon or nitrogen. Once each layer is distributed, each 2D slice of the part geometry is fused by selectively melting the powder. The process is repeated layer by layer until the part is complete [26]. The cubic samples (8 × 8 × 8 mm^3) were fabricated under different process-parameter combinations until optimisation was achieved; the optimum parameters were then employed to fabricate the tensile specimens. Table 1 shows the used SLM process parameters for optimisation. The criterion employed to achieve the parameters optimisation is the density based on the Archimedes principle; No. 7 and 14 (Table 1) were determined to be the optimal parameters to fabricate pure HX and the nanocomposite samples in

the present study. Note that the substrate was not preheated before the build, and the tensile specimens were manufactured horizontally where the loading direction was perpendicular to the build direction. The shape and dimensions of the specimens were determined based on ASTM-E8/E8M-13a [27]. Although the vertically manufactured specimens exhibited higher tensile strength and toughness compared to the horizontally fabricated parts [22], the vertical manufacture scenario requires much more powder to fill the build volume. The horizontal manufacture strategy was thus employed in this work.

Table 1. The used SLM parameters in this study.

Laser power (P) = 200 W, Layer thickness (t) = 40 μm					
No.	Scanning speed (v, mm/s)	Hatch spacing (h, μm)	No.	Scanning speed (v, mm/s)	Hatch spacing (h, μm)
1	300	80	9	800	100
2	400	80	10	1000	100
3	600	80	11	300	120
4	800	80	12	400	120
5	1000	80	13	600	120
6	300	100	14[†]	800	120
7[†]	400	100	15	1000	120
8	600	100			

[†]No.7 and 14 are the optimised parameters.

2.3. Material characterisation techniques

Both pure HX and nanocomposite samples were vertically sectioned parallel to the build direction and then ground and polished using standard techniques prior to optical microscopy (OM, Nikon S-Ke type, Japan) and scanning electron microscopy (SEM, Carl ZEISS EVO 40, Germany) inspections, as detailed in previous studies [28][29]. All samples were examined in the as-fabricated condition without any post-processing treatments. For the microstructure analysis, to reveal the rapid solidification structures and molten-pool boundaries, the polished cubic specimens were subjected to electrochemical etching for 10 s in oxalic acid. The samples for backscattered electron (BSE) SEM and electron backscatter diffraction (EBSD) analysis were polished only, without chemical etching.

The EBSD analysis was performed using a high resolution Jeol 7800F FEG-SEM equipped with an Oxford Instruments Aztec EBSD system, to study the crystallographic orientation of the samples. The EBSD scanning was operated under 20 kV and was performed on an area of 1 × 1 mm^2, with a step size of 0.8 μm. Post-data processing was conducted using the HKL Channel 5 EBSD software package. The optimum process parameters were determined by measuring the relative density of the as-fabricated cubic samples three times and then averaging those values based on the Archimedes principle. Transmission electron microscopy (TEM) inspection was performed to further examine the microstructure of the nanocomposite sample. TEM characterisation was performed with an FEI Titan Themis 80–300 equipped with two aberration correctors and a highly efficient (four-quadrant) energy-dispersive X-ray (EDX) system. Uniaxial tensile testing was performed using a Zwick/Roell tester (Z050, Ulm, Germany) with a maximum load of 100 kN and a strain rate of 1.33×10^{-3} s^{-1} at room temperature. The engineering stress-strain curves obtained from that process were determined from two specimens for both conditions (pure HX and nanocomposite materials).

3. Results

3.1. Relative density and defects distribution

Fig. 2a shows the measured density of both pure HX and HX-3 wt. % TiC nanocomposite versus laser-energy density. The laser-energy density was calculated using the formula $\varepsilon = P/(v \cdot h \cdot t)$, where P represents the laser power and v, h and t denote the scanning speed, hatch spacing and layer thickness, respectively. This is a commonly used method by other researchers to estimate the correlation between manufacture condition and the porosity of SLM-fabricated parts [30][31]. The relative density was determined in the present study by measuring the density of the cubic samples three times using the Archimedes method and then averaging the values. Both materials showed a trend in which relative-density values increased alongside increased energy density until the maximum relative density was achieved; the relative density decreased with further increases in energy density. The highest relative density of SLM-fabricated pure HX was measured to be 99.5% when a 52.08 J/mm^3 laser-energy density was employed; this point corresponded to laser power = 200 W, scanning speed = 800 mm/s, hatch spacing = 120 μm and layer thickness = 40 μm.

Both the laser-power and layer-thickness values remained fixed in the present study, while we optimised the scanning-speed and hatch-spacing variables to achieve the optimal manufacture condition.
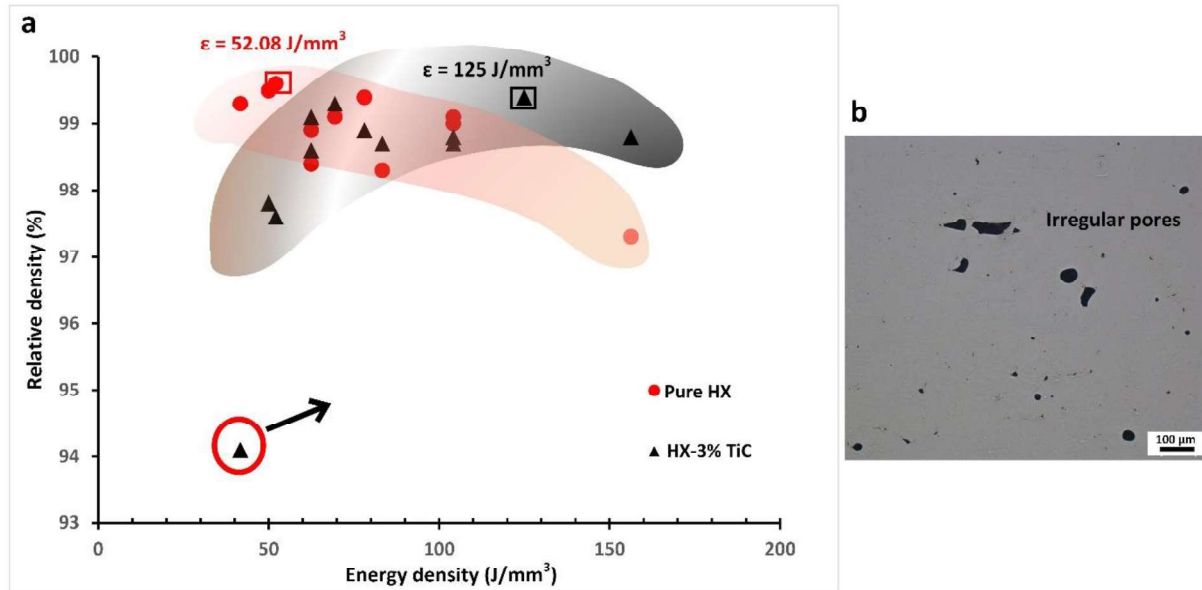

Fig. 2. The relative density of pure HX and HX-3 wt.% TiC nanocomposite: (a) relative density versus laser-energy density; (b) a typical optical micrograph showing irregular pores under insufficient laser-energy density.

Compared to the pure HX material, the nanocomposite material required a higher laser-energy density (125 J/mm^3) to achieve a relative density above 99.3%. The optimised parameters used to manufacture the highest-density nanocomposite samples included laser power = 200 W, scanning speed = 400 mm/s, hatch spacing = 100 μm and layer thickness = 40 μm. Particularly when the energy density employed was below 50 J/mm^3, the relative density was measured to be only around 94%, whereas this value increased to 97.5% and even higher when the energy density was greater than 50 J/mm^3. This finding suggests that insufficient melting occurred in the SLM of nanocomposite material when the energy density was below 50 J/mm^3. This lack of melting may have caused the formation of irregular pores in the parts, as confirmed by the microstructure analysis (Fig. 2b).

Fig. 3 shows the defect distribution and molten-pool boundaries in the as-fabricated HX and nanocomposite samples built under optimal conditions. Microcracks were found to be the primary defects and were uniformly distributed in the pure HX, with a defect density of about 0.5%, even under the optimum build condition. The length of the cracks varied from several micrometres to more than 100 micrometres, implying that the microcracks propagated to a few solidified layers along the build direction (Fig.

3a). Compared to pure HX, a few residual pores with a volume fraction of around 0.6% were detected in the nanocomposite, but no microcracks were detected under OM inspection (Fig. 3c). When subjected to a proper etching, the solidified molten-pool boundaries were revealed; the nanocomposite was found to have exhibited wider and shallower molten pools compared to the pure HX (Fig. 3b/d). The microcracks in the pure HX did not form on the molten-pool boundaries; instead, they crossed the boundaries and propagated along the build direction (Fig. 3b).
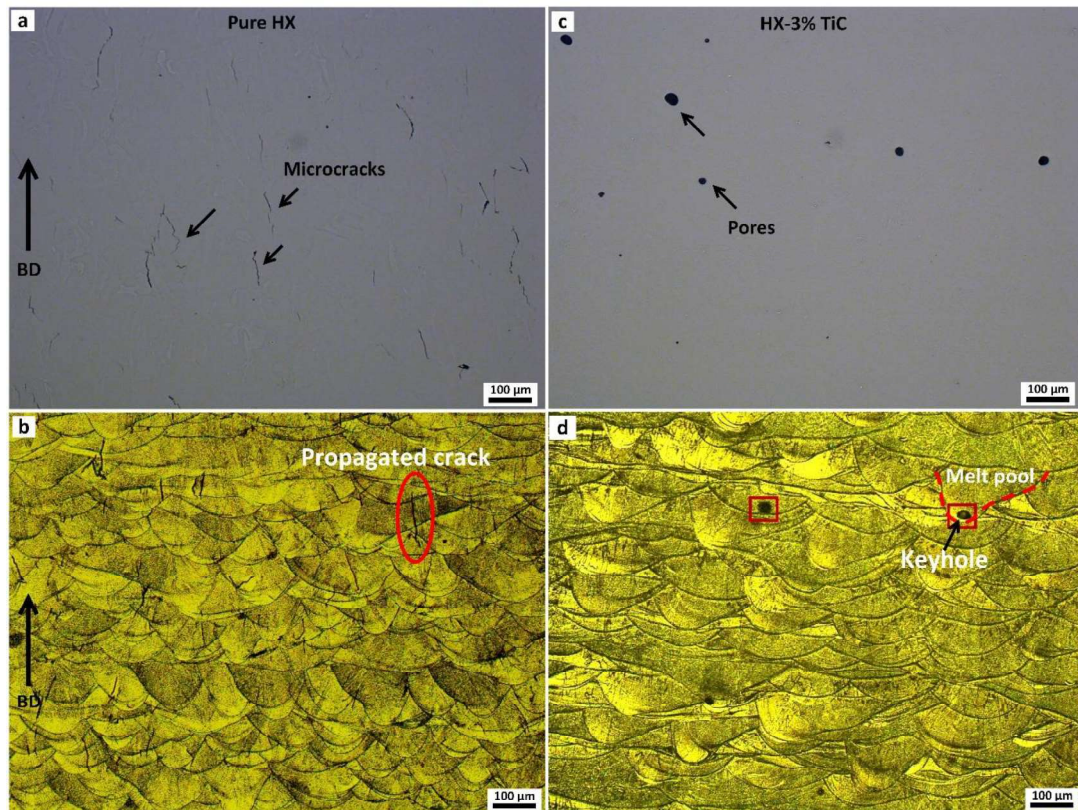

Fig. 3. Defect distribution and molten pools in the built samples under optimum conditions: (a)-(b) pure HX; (c)-(d) nanocomposite material.

Interestingly, a very limited number of keyhole pores were observed in the nanocomposite but were not detected in the pure HX (Fig. 3d). This finding may be linked to the higher laser-energy density employed in the nanocomposite, but the majority of the molten pools in the nanocomposite were very shallow. Keyhole pores did not form in these cases, because such pores are generally accompanied by hopper-like molten pools [32][33]. The implication of this situation is that the TiC nanoparticles in the present study may not have been uniformly dispersed in the fabricated nanocomposite sample, so several nanoparticles could have agglomerated and formed clusters during the SLM process. These properties were further

investigated via high-resolution BSE SEM and EDX inspections, as noted in the following section.

3.2. Microstructure

Fig. 4 shows BSE-SEM images of both pure HX and nanocomposite samples under optimum manufacture conditions. These images are useful for the investigation of the effects of TiC nanoparticles on microstructure and mechanical property alteration. Fig. 4a-b reveal the columnar grains that formed along the build direction in the pure HX. More specifically, the grains grew along the positive temperature gradients during the SLM process and crossed the fusion boundaries to form columnar grains. The temperature gradients formed because of the high-energy laser beam, in which a Gaussian distribution was used. The microcracks were observed to be distributed along the grain boundaries, implying that the cracks that formed were intergranular rather than transgranular in the pure HX. Numerous previous studies have examined the formation mechanism of intergranular cracks in SLM-fabricated HX alloy; element segregation and residual thermal-stress accumulation are generally considered to be the primary contributors to microcrack formation [20][34][35].
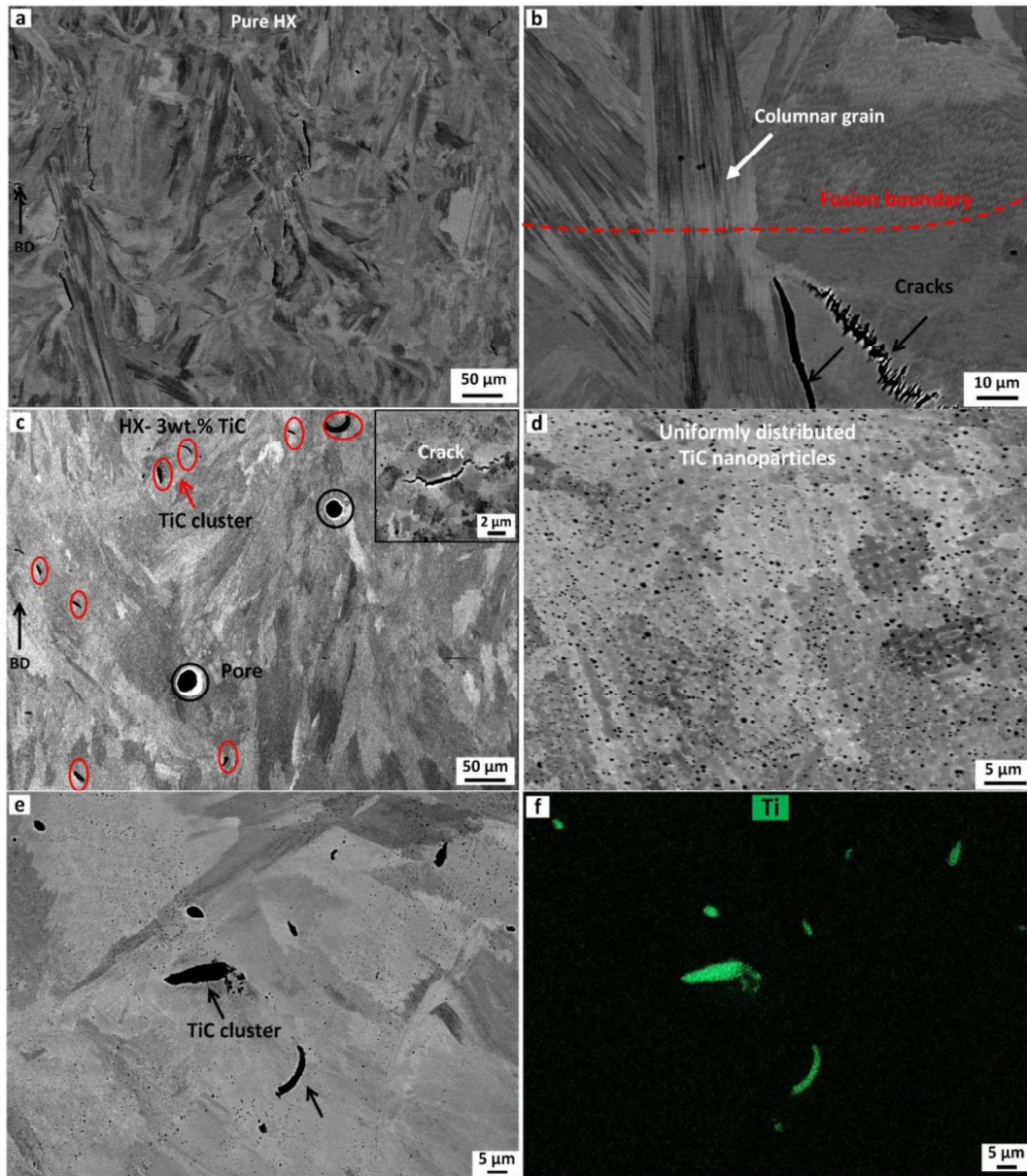
Fig. 4. Backscattered electron (BSE) SEM images showing the microstructure of as-fabricated pure HX and nanocomposite samples: (a)–(b) microstructure and microcracks in pure HX; (c)–(d) microstructure and uniformly distributed TiC in the nanocomposite; (e)–(f) agglomerated TiC clusters in the nanocomposite sample.

Compared to pure HX, the nanocomposite was not found to have formed intergranular cracks, indicating that the added 3 wt.% TiC nanoparticles enabled the elimination of microcracks formed during the SLM process (Fig. 4c-d). Despite the removal of intergranular cracks, however, the TiC-reinforced nanoparticles resulted in open pores with a size generally greater than 30 μm in diameter and irregularly shaped defects that were found to be TiC clusters (Fig. 4e-f). Those TiC clusters with irregular shapes were smaller than open pores, and their formation may be attributable to the

Marangoni effect within the SLM process, which in this study drove the nanoparticles to form several clusters, while the nanoparticle fraction was above a threshold.

Another contributor could have stemmed from the imperfect HX particles from the feedstock, which typically exhibits defects such as cavities or satellite particles. The HX powder used in this study was recycled powder, so these cavity defects and satellite particles could have trapped the nanoparticles during high-speed mixing and hinder the uniform dispersion of TiC nanoparticles amongst HX particles. The trapped TiC clusters could not be dispersed by the Marangoni effect, and the cluster defect formed. This finding indicates that the spherical gas-atomised particles should offer as few defects as possible when processing high-quality and defect-free components via the SLM process. TiC-cluster defects are very likely to function as stress-concentration sites and to lead to the formation of microcracks during the SLM solidification stage. Very few transgranular microcracks were observed in the nanocomposite sample, but the formation mechanism differed from that of the intergranular microcracks. We should note that, apart from the TiC clusters, most of the TiC nanoparticles were evenly distributed in the matrix, and no interface defect was observed (Fig. 4d). These uniformly distributed TiC particles were able to improve the mechanical strength of SLM-fabricated nanocomposite specimens.

Fig. 5 shows the EDX mapping of a zone from the HX-3 wt.% TiC nanocomposite specimen; this information is useful to understand the effects of TiC nanoparticles on microcrack elimination. The EDX mapping confirmed that the added TiC nanoparticles were uniformly distributed in the HX matrix following solidification; chemical reactions between TiC and other alloying elements were not found to have occurred as expected. As a typical SLM solidification structure, columnar walls surrounded by precipitates formed in the fabricated sample. The segregated phase was found to include Mo- and Cr-rich carbides. Previous studies have also detected segregation in SLM-fabricated pure HX alloy, as reported in [21][25], indicating that the added TiC nanoparticles in the present study were incapable of stopping the element segregation in the SLM of HX-based nanocomposites. Considering the two primary contributors to microcracking, since previous studies have found segregation to occur in both pure HX and HX-based nanocomposite (which increases hot-tearing susceptibility), thermal residual stress must play a significant role in microcrack formation in the SLM of pure HX. The added 3 wt.% TiC nanoparticles in the present study were very likely to have somehow

degraded the residual stress accumulation, since intergranular microcracks had been eliminated in the fabricated nanocomposite sample.
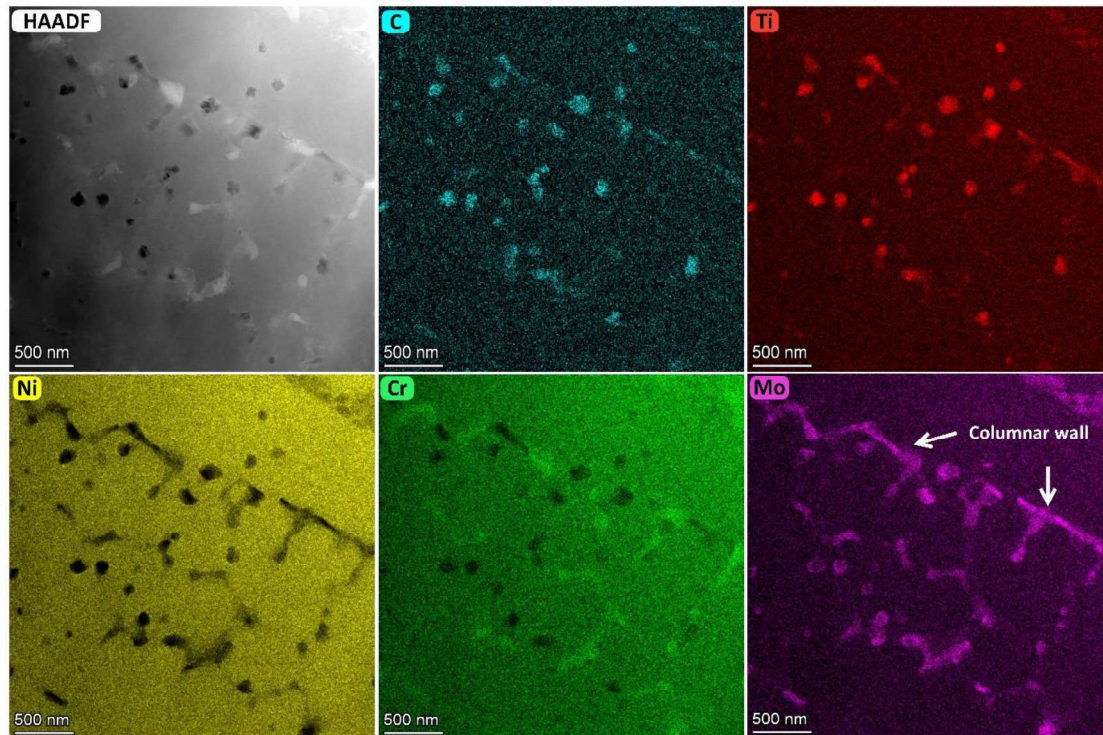

Fig. 5. Compositional mapping of a zone from the nanocomposite sample.

Fig. 6 shows the EBSD inverse pole figure (IPF) mapping of the as-fabricated pure HX and HX-3 wt.% TiC nanocomposite samples. The random grain orientations instead of the (001) orientation imply a relatively weak texture in the pure HX. This finding differs from those of previous studies, where the (001) orientation was the preferential grain-growth orientation for face-centred cubic (FCC) structure materials [36][37]. In the present study, the grains in the pure HX grew along the direction of heat flow to form epitaxial grains (Fig. 6a). In addition, the EBSD inspection confirmed that the microcracks that formed in pure HX were intergranular, as they were distributed along the high-angle grain boundaries (Fig. 6c). Compared to the pure HX, the added 3 wt.% TiC nanoparticles contributed to a strong (001) orientation for the columnar grains that formed (Fig. 6b).

Using 1 mm × 1 mm regions taken from the IPF orientation maps for both samples, the aspect ratio (AR) of the fitted ellipses' length-over-width value for the grains was calculated, as shown in Fig. 6d. A higher length-over-width AR indicates a more columnar grain, while a value of 1 represents a perfectly circular fitted shape. The calculated number of grains in the measured regions were 4,484 and 5,402 for pure

HX and nanocomposite, respectively. The significantly increased grains in the nanocomposite indicate that the added 3 wt.% TiC nanoparticles had resulted in grain refinement in the nanocomposite. In particular, the effects seemed to be more influential on grain-width refinement (Fig. 6b). Under the AR range of 1–2, the number of grains in the pure HX and nanocomposite were found to be 804 and 1,503, respectively. When the AR range increased to 2–5, the nanocomposite underwent another increase by 700 relatively circular grains compared to pure HX. We may conclude that the TiC nanoparticles functioned as a heterogeneous nucleation agent and promoted nucleation, which generated fine grains. With further increases in AR (value > 5), where a value of 5 generally represents typical epitaxial grains, pure HX underwent the formation of more columnar grains than the nanocomposite.

Fig. 6. EBSD images of as-fabricated pure HX and nanocomposite samples: (a) IPF orientation map for pure HX; (b) IPF orientation map for the nanocomposite; (c) IPF map showing intergranular cracks in pure HX; (d) number of grains compared to aspect ratio (AR) in both samples.

The grain refinement enabled more grain boundaries in the nanocomposite sample, which may have strengthened the cohesion of the grain boundaries. We may conclude

that the extra grain boundaries induced by the TiC nanoparticles played a crucial role in intergranular microcrack elimination.

In addition to microcrack elimination, the added 3 wt.% TiC nanoparticles enhanced the mechanical strength of the SLM-fabricated nanocomposite. The grain-refinement strengthening was very likely to be a significant strengthening mechanism in this composite, based on Hall-Petch theory [38]. Fig. 7 shows bright-field TEM images of as-fabricated HX-3 wt.% TiC nanocomposite; these images are useful for the investigation of the nanoparticles' reinforcing mechanism. The zone near the interface of TiC reinforcements and the matrix was found to exhibit a higher dislocation density compared to other areas in the matrix (Fig. 7a-b), implying that the enhanced dislocation-density strengthening would be a non-negligible mechanism for improving mechanical strength. The significant increase in dislocation density occurred because of the mismatch of the coefficient of thermal expansion (CTE) between the matrix and the TiC nanoparticles. The CTE values for TiC and HX at room temperature are 7.7×10^{-6} m/m-°C and 13.9×10^{-6} m/m-°C, respectively. A previous study has found that the contribution of CTE mismatch was significant in SLM-fabricated nanocomposite materials, because the CTE difference between the matrix and ceramic nanoparticles increased with temperature, which led to an increase in dislocation density near the interface [4]. Selected area electron diffraction (SAED) was conducted to analyse the phase formed amongst the matrix after rapid solidification. The irregular precipitates that formed were clearly observed in the matrix and the SAED analysis confirmed that the precipitated carbide phase was $M_{23}C_6$, which generally has a lower melting temperature compared to the matrix material (Fig. 7c-d). This phase analysis shows agreement with the EDX mapping (Fig. 5) that the formed columnar walls were rich in Mo and Cr elements. In addition, since TiC nanoparticles have been observed uniformly distributed in the matrix and the formed precipitated phase was examined to be $M_{23}C_6$, indicating that no interfacial reactions occurred between TiC nanoparticles and the austenite matrix.

Fig. 7. Bright-field TEM images of HX-3 wt.% TiC nanoparticles: (a)-(b) TEM images showing the effects the TiC nanoparticles on dislocation density; (c)-(d) brightfield TEM image and corresponding SAED patterns for the precipitated phase; (e)-(f) TEM images showing the TiC nanoparticles distribution and strong interface;.

Fig. 7e-f show strong bonding between TiC and the HX matrix, with no defects observed at the interface. The d-spacing was measured to be 0.25 nm, indicating the

TiC nanoparticles were embedded in the matrix. Since the temperature induced by the laser irradiation was below the melting-point temperature of TiC, the HX was fully melted and solidified rapidly, while the TiC nanoparticles remained in solid state. Strong bonding at the atomic level between TiC and the matrix was achieved due to the nanoscale connection and rapid solidification. The strong coherent bonding was expected to facilitate the load transfer at the interface and further increase the strength of the nanocomposite material. This bonding suggests that load-bearing strengthening would be another mechanism that could enhance the mechanical strength of the SLM-fabricated nanocomposite material. We should note, however, that the TiC cluster defects induced by the nanoparticle agglomeration resulted in the loss of interphase cohesion, which is generally detrimental to strength improvement [39]. Considering the present study's preparation method of the nanocomposite feedstock through high-speed mixing, which is a typical ex situ processing technique, an effective in situ processing method might facilitate finer and more thermodynamically stable particles with more uniform size distribution in the matrix to minimise interface defects.

3.3. Tensile performance

Fig. 8 shows the tensile properties of as-fabricated pure HX and nanocomposite specimens as well as a comparison with results reported in the literature. Tensile performance was measured using uniaxial tensile testing at room temperature. The tensile behaviours of the two pure HX specimens were found to be consistent, with a 690 ± 4 MPa yield strength, 920 ± 2 MPa ultimate tensile strength (UTS) and 13 ± 2% elongation to failure (Fig. 8a). Compared to pure HX alloy, the nanocomposite materials exhibited approximately 140 MPa and 230 MPa higher yield strength and UTS, respectively, while the elongation to failure was not detected to exhibit an obvious decrease; the elongation was measured to be 12 ± 1.4%. The remarkable increase in tensile performance can be attributed to the addition of 3 wt.% TiC nanoparticle reinforcements, which eliminated the intergranular microcracks in HX during the SLM process. Table 2 shows the tensile performance of the as-fabricated pure HX, HX-3 wt.% TiC nanocomposite and HX-1 wt.% TiC nanocomposite from the previous work [25]. It should be noted that the strength of the crack-free HX-1 wt.% TiC nanocomposite from [25] was slightly lower compared to the as-fabricated pure HX in this study which suffered from hot cracking. This difference in mechanical performance could be explained by the slight difference in the chemical composition

of the HX materials used; in particular, the carbon content was found to have a significant effect in mechanical strength enhancement of the SLM-fabricated HX [20]. Indeed, the carbon content in this study was measured to be 0.13 wt.% while the value was 0.06 wt.% in the previous work [25].
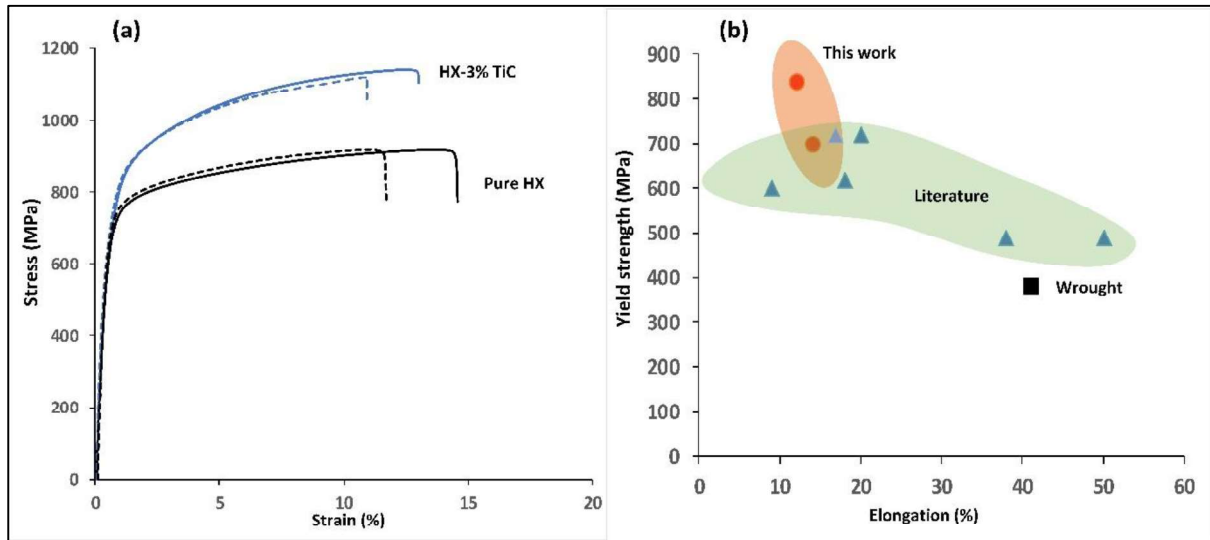

Fig. 8. Tensile properties of as-fabricated pure HX and nanocomposite materials: (a) representative engineering stress-strain curves of the as-fabricated materials in this study; (b) yield strength (0.2% offset) versus tensile elongation to failure for HX alloy reported in the literature [19][22][23] [25][34][40].

Table 2. Tensile performance of as-fabricated HX materials.

Material	Yield strength (MPa)	UTS (MPa)	Elongation (%)
Pure HX	690± 4	920± 2	13± 2
HX-3 wt.% TiC	830± 2	1150± 3	12± 1.4
HX-1 wt.% TiC (previous work)	682± 5.6	849± 1	15± 4.2

The 'yield strength' vs 'tensile elongation to failure' values for HX alloy reported in the present study compared to the literature are shown in Fig. 8b. The SLM-manufactured HX exhibited a higher yield strength of over 100 MPa compared to wrought HX alloy because of the specialised layer-by-layer and rapid-cooling manufacture principle of additive manufacturing (AM). Note that for the as-fabricated HX alloy, the reported yield strength from different types of AM equipment varied from 500 MPa to 700 MPa, while the elongation to failure varied from about 10% to 50%, suggesting that the mechanical performance of SLM-fabricated HX could depend on different AM machines and process parameters. Another significant contributor is the

difference in chemical composition between the raw HX powders [41]. For instance, the nominal percentage range of the carbon (C) element in HX is 0.05–0.15%, based on ASTM standards. The increase in C content can improve tensile strength, but ductility might be sacrificed.

The yield strength of HX-3 wt.% TiC nanocomposite we obtained in this study was superior compared to the reported wrought- and SLM-fabricated HX, but the TiC clusters and newly formed microcrack defects, together with the formed open pores resulted in the degradation in both tensile strength and ductility to some degree. In addition, the pores and microcrack defects that located nearby the sample surface may act as the stress-concentration sites at the crack initiation stage and further to accelerate the failure when subjected to fatigue testing. It is anticipated that further improvements to ductility could be achieved through the careful manipulation of the raw HX powder and the amount of TiC reinforcement used.

Fig. 9 shows typical micrographs of the tensile specimens from both materials after tensile testing. The intergranular microcracks were further opened under uniaxial loading, and several cleavage-like fractures formed in the pure HX alloy (Fig. 9a-c). Cleavage fracturing generally indicates a brittle fracture and stems from tiny defects such as microcracks, inclusions and the lack of fusion in SLM-fabricated parts, all of which induce high-stress triaxiality but are easily ignored [42].

Fine dimples were observed in the fracture surfaces, suggesting a ductile fracture at the crack-free areas. This finding indicates that the fracturing found in the as-fabricated pure HX was a combination of both brittle and ductile fractures, which eventually contributed to a 14% elongation to failure (Fig. 8a). In contrast, the fracture surface of the nanocomposite sample was smoother than that of pure HX, whereas a few pores and small cracks had formed. The length and width of the cracks that formed in the nanocomposite were much smaller than the opened cracks in pure HX. The micro-voids (void size of < 1 μm) that formed with coalesced dimples implied a ductile fracture of the nanocomposite sample (Fig. 9d-f).
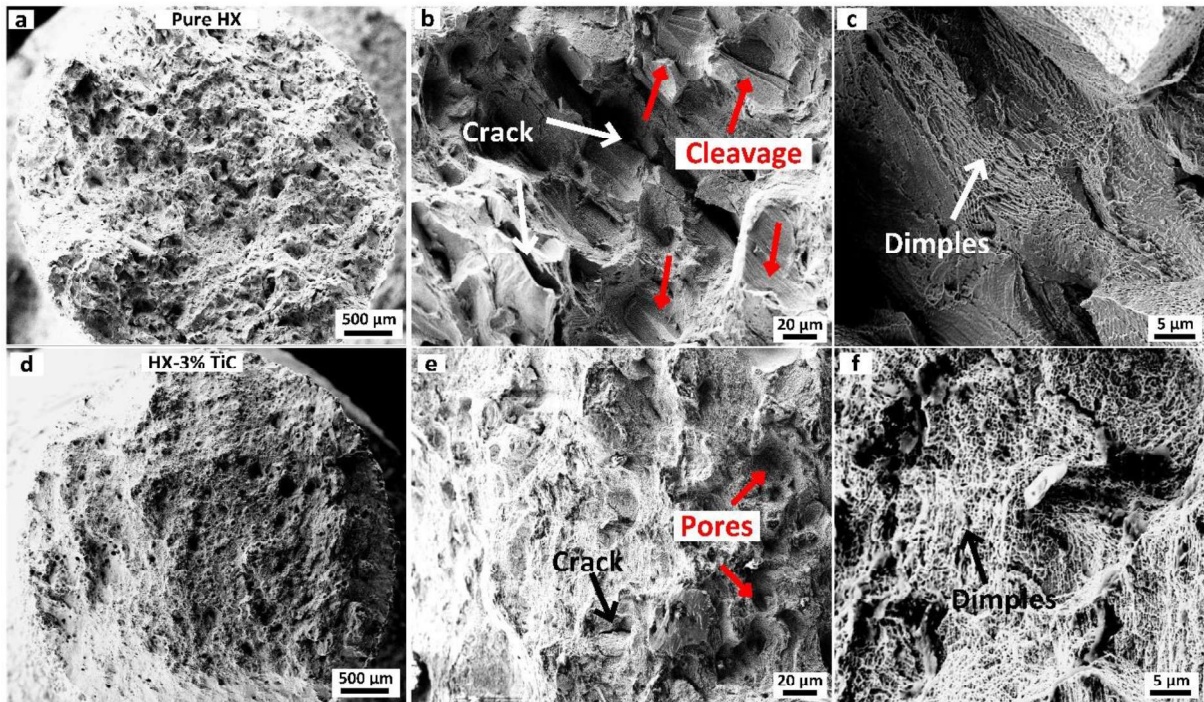
Fig. 9. SEM micrographs showing the fracture surfaces of as-fabricated samples: (a)–(c) pure HX alloy; (d)–(f) HX-3 wt.% TiC nanocomposite.

4. Discussion

4.1. The effect of TiC addition on thermophysical properties

When comparing the optimal laser-energy density between the pure HX and HX-3 wt.% TiC nanocomposite, a finding that should be mentioned relates to the added 3 wt.% TiC nanoparticles, which significantly increased the laser-energy density before achieving a nearly full-density nanocomposite manufactured via SLM. This achievement can be explained by the physical properties changed by the added nanoparticles. The nanocomposite feedstock increased in laser absorption compared to the pure HX feedstock because of the increment of surface roughness, which led to multiple reflections and numerous absorptions of the laser [43][44]. From the laser-absorption perspective, the nanocomposite was expected to enable a lower laser-energy density being necessary compared to pure HX material. The added TiC nanoparticles, however, also changed the effective thermal conductivity of the nanocomposite feedstock. Previous studies have demonstrated that nanoparticles decrease thermal conductivity, whether they exhibit a higher or lower thermal conductivity compared to the matrices, because they introduce interfacial thermal resistance and scatter the energy carriers (electrons and phonons) [4][45][46]. In

general, reductions in the thermal conductivity of both powder and the bulk system result in slower heat conduction among nanocomposite powders and in the solidified bulk layers during SLM. In the present study, the addition of 3 wt.% TiC ceramic particles reduced the thermal conductivity of both powder feedstock and solidified bulk layers so that a higher laser-energy density was required to fabricate the nearly full-density nanocomposite.

Considering the above changes in both laser absorption and thermal conductivity, the added 3 wt.% TiC nanoparticles in this study seemed to be more influential on the effective thermal conductivity than the laser-absorption aspect. This is because an extra 73 J/mm^3 laser-energy density was required to fabricate the full-density nanocomposite compared to the pure HX material.

4.2. Possible strengthening mechanisms

The experimental results from this study have demonstrated that microcracking is the primary defect within the SLM of HX alloy. The microcracks could not be eliminated even under the optimal manufacture conditions, where the crack density was about 0.5%. The addition of 3 wt. % TiC nanoparticles was found to not only enhance tensile strength but also to eliminate intergranular microcracks. Available studies in the literature have revealed possible strengthening mechanisms in tensile strength by the introduction of a nanoscale reinforcement phase, such as the Orowan, load-bearing and CTE mismatch strengthening mechanisms [47][48][49][50]. Based on the tensile strength analysis, the addition of 3 wt.% TiC nanoparticles contributed to about 140 MPa increase in yield strength, while Orowan dislocation rings have not been observed via the TEM analysis (Fig. 7a), indicating the Orowan strengthening may not be the key strengthening mechanism in the HX-3 wt.% nanocomposite. The CTE mismatch strengthening can be estimated by $\Delta_{\sigma CTE} = M\beta G_m b\sqrt{\rho_{CTE}}$ [38], where M is the Taylor factor, β is the dislocation strengthening coefficient, G_m is the shear modulus of the matrix, b is the magnitude of Burger's vector and ρ_{CTE} is the density of dislocations generated from the CTE difference. The estimated $\Delta_{\sigma CTE}$ is determined to be over 80 MPa in this study. In addition, a large number of strong interfaces without apparent interfacial defects have been formed between the matrix and the 3 wt.% TiC nanoparticles (Fig. 7e-f), indicating that the load-bearing strengthening is another significant strengthening mechanism in the as-fabricated nanocomposite.

4.3. Microcracking formation and elimination mechanisms

Another interesting finding in this research was the elimination of microcracks by the added TiC nanoparticles, as illustrated in Fig. 10. Within the SLM of pure HX, the rapid cooling rate of up to 10^6 K/s resulted in element segregation to form carbides [19]. Our experimental results and results from the available literature both confirm that the segregated materials were Mo- and Cr-rich carbides [21][24]. The addition of the C element, which was 0.13 wt.% in the HX, strengthened the endurance properties of HX, because those carbides that formed and were dispersed inside grains and on grain boundaries functioned as a reinforcement phase to strengthen the grain boundaries. The carbides on the grain boundaries, however, made the grain boundaries more susceptible to hot cracking. Considering the significant temperature gradient and cooling rate induced by laser irradiation, and because thermal residual stresses constantly accumulated as the build continued, intergranular microcracks could have formed if the thermal stress had been greater than the ultimate tensile strength of the grain boundaries at that temperature.
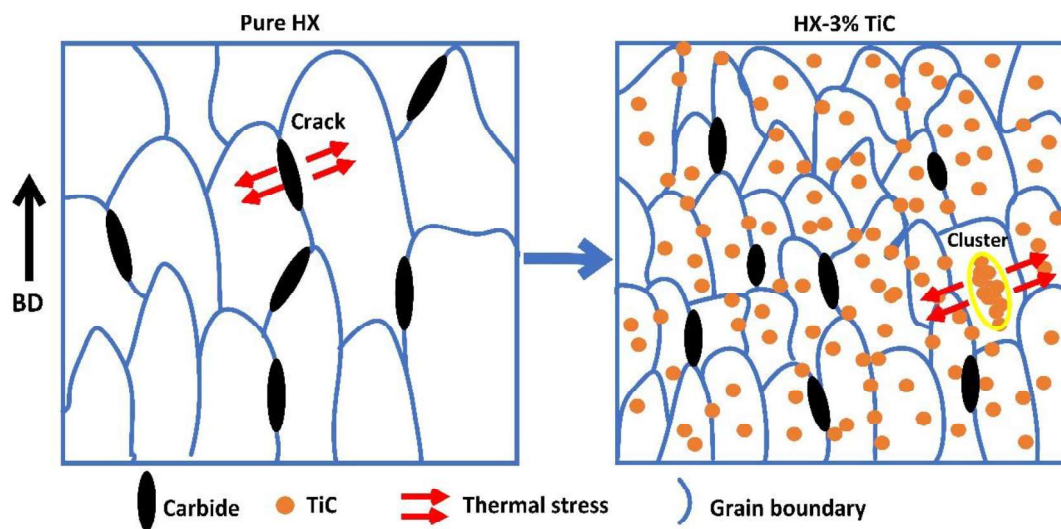

Fig. 10. Schematic illustration of microcrack elimination by the addition of TiC nanoparticles.

Segregation was still detected in the SLM-fabricated nanocomposite, which indicates that the added nanoparticles were unable to prevent element segregation. The microcrack elimination thus may have been caused by reductions in thermal stresses. Our EBSD analysis has demonstrated that the grains formed in the nanocomposite were smaller than those in pure HX. In particular, the reduction in grain width was found to have been more influential, which indicates that the added 3 wt.%

TiC nanoparticles enabled grain refinement and an increasing of grain boundaries in the nanocomposite. This situation probably occurred because the TiC particles functioned as heterogeneous nucleation sites, as confirmed by the uniform distribution of the majority of the nanoparticles found in the HX matrix. The significantly increased grain boundaries were capable of strengthening the grains' adhesion because the feeding of molten material is always easier to accomplish at the grain boundaries compared to the interdendritic areas. In addition, the large number of grain boundaries made the strains caused by the thermal stresses to be uniform. The hot cracking was thus eliminated, even though the segregation took place in the nanocomposite. This finding is also consistent with that of a previous study, which found that an increase in grain boundaries contributed to hot-tearing resistance in the casting of nickel-based superalloys [51].

A limited number of transgranular microcracks were detected in the present study's nanocomposite sample. This microcracking was more likely to have been induced by the TiC clusters. The defect was not detected in the authors' previous study, however, where 1 wt.% TiC nanoparticles were added to enhance the HX alloy [25]. In addition, in terms of the BSE-SEM inspection, the TiC nanoparticles were not found to have uniformly distributed in the 'with-defect' areas in the nanocomposite; some were located along the grain boundaries and some tended to form clusters (Fig. 4e). One possible explanation might be that the non-uniformly coated TiC nanoparticles changed the thermophysical properties of the nanocomposite powder feedstock, which further induced unstable molten pools and some TiC nanoparticles were pushed to be located along the grain boundaries. Another contributor could be the poor wettability of the TiC ceramic particles when the content was above the allowed threshold so that the TiC nanoparticles were non-uniformly distributed in the HX matrix after the rapid solidification. The situation suggests that the added 3 wt. % TiC nanoparticles may have sufficiently reached the threshold of the allowable reinforcement content, such that the Marangoni force caused by surface tension was not strong enough to separate the nanoparticles during the liquid-solid-phase transformation.

5. Conclusions

This study has investigated the effects of TiC nanoparticles on microcrack elimination and tensile-strength enhancement in Hastelloy X (HX)-based nanocomposite fabricated by selective laser melting (SLM). The experimental study explored the possible hot-cracking formation principle and elimination mechanism by the added nanoparticles and showed the following findings.

(1) An extra 73 J/mm^3 laser-energy density was required to fabricate nearly full-density nanocomposite samples compared to pure HX alloy. This finding indicates that the added 3 wt.% TiC nanoparticles were more influential in the feedstock's thermal-conductivity reduction than the increase in laser absorptivity.

(2) Intergranular microcrack elimination was achieved in the SLM-fabricated nanocomposite material due to the addition of TiC nanoparticles. The increased grain boundaries induced by grain refinement were found to have been the primary contributor, because they were capable of strengthening the grains' adhesion and to make the strains caused by thermal residual stresses uniform.

(3) The addition of 3 wt.% TiC nanoparticles contributed to an approximately 17% increase in yield strength in the nanocomposite material, while the elongation to failure was not found to show significant reduction compared to the pure HX alloy. Our microstructure examination revealed that the strengthening mechanisms of grain refinement, load bearing and enhanced-dislocation density were very likely to be the most pronounced mechanisms in the SLM-fabricated HX-3 wt.% TiC nanocomposite.

These findings indicate that titanium carbide nanoparticles facilitated hot-cracking elimination and tensile-strength enhancement in the SLM of the HX superalloy. We expect that this significant finding will accelerate the adoption of the additive manufacturing of high-performance and defect-free nickel-based superalloys in the aerospace industry and other applications. The 3 wt.% TiC nanoparticles, however, led to the formation of a limited number of TiC clusters and transgranular microcracks, which was detrimental to the material's mechanical and physical properties. We anticipate that further improvements to cluster elimination could be achieved through the careful manipulation of the raw HX powder and the amount of TiC reinforcement used in the process.

Acknowledgements

Declaration of interest statement

The authors have no conflict of interest.

Data availability statement

The raw/processed data required to reproduce these findings cannot be shared at this time as the data also forms part of an ongoing study.

References

[1] Yang L, Zhicong P, Ming L, Yonggang W, Di W, Changhui S, et al. Investigation into the dynamic mechanical properties of selective laser melted Ti-6Al-4V alloy at high strain rate tensile loading. Mater Sci Eng A 2019;745:440–9. https://doi.org/10.1016/j.msea.2019.01.010.

[2] Wang M, Song B, Wei Q, Zhang Y, Shi Y. Effects of annealing on the microstructure and mechanical properties of selective laser melted AlSi7Mg alloy. Mater Sci Eng A 2019;739:463–72. https://doi.org/10.1016/j.msea.2018.10.047.

[3] Han Q, Gu H, Soe S, Setchi R, Lacan F, Hill J. Manufacturability of AlSi10Mg overhang structures fabricated by laser powder bed fusion. Mater Des 2018;160:1080–95. https://doi.org/10.1016/j.matdes.2018.10.043.

[4] Yu WH, Sing SL, Chua CK, Kuo CN, Tian XL. Particle-reinforced metal matrix nanocomposites fabricated by selective laser melting: A state of the art review. Prog Mater Sci 2019;104:330–79. https://doi.org/10.1016/j.pmatsci.2019.04.006.

[5] Zhang LC, Attar H. Selective Laser Melting of Titanium Alloys and Titanium Matrix Composites for Biomedical Applications: A Review. Adv Eng Mater 2016;18:463–75. https://doi.org/10.1002/adem.201500419.

[6] Ataee A, Li Y, Brandt M, Wen C. Ultrahigh-strength titanium gyroid scaffolds manufactured by selective laser melting (SLM) for bone implant applications. Acta Mater 2018;158:354–68. https://doi.org/10.1016/j.actamat.2018.08.005.

[7] Martin JH, Yahata BD, Hundley JM, Mayer JA, Schaedler TA, Pollock TM. 3D printing of high-strength aluminium alloys. Nature 2017;549:365–9. https://doi.org/10.1038/nature23894.

[8] Catchpole-Smith S, Aboulkhair N, Parry L, Tuck C, Ashcroft IA, Clare A. Fractal scan strategies for selective laser melting of 'unweldable' nickel superalloys. Addit Manuf 2017;15:113–22. https://doi.org/10.1016/j.addma.2017.02.002.

[9]   Li J, Zhao Z, Bai P, Qu H, Liu B, Li L, et al. Microstructural evolution and mechanical properties of IN718 alloy fabricated by selective laser melting following different heat treatments. J Alloys Compd 2019;772:861–70. https://doi.org/10.1016/j.jallcom.2018.09.200.

[10]   Zhao JC, Larsen M, Ravikumar V. Phase precipitation and time-temperature-transformation diagram of Hastelloy X. Mater Sci Eng A 2000;293:112–9. https://doi.org/10.1016/S0921-5093(00)01049-2.

[11]   Moya JS, Lopez-Esteban S, Pecharromán C. The challenge of ceramic/metal microcomposites and nanocomposites. Prog Mater Sci 2007;52:1017–90. https://doi.org/10.1016/j.pmatsci.2006.09.003.

[12]   Shuai C, Wang B, Bin S, Peng S, Gao C. TiO2-Induced in Situ Reaction in Graphene Oxide-Reinforced AZ61 Biocomposites to Enhance the Interfacial Bonding. ACS Appl Mater Interfaces 2020;12:23464–73. https://doi.org/10.1021/acsami.0c04020.

[13]   Sajjadi SA, Ezatpour HR, Beygi H. Microstructure and mechanical properties of Al-Al2O3 micro and nano composites fabricated by stir casting. Mater Sci Eng A 2011;528:8765–71. https://doi.org/10.1016/j.msea.2011.08.052.

[14]   Gao C, Yao M, Shuai C, Peng S, Deng Y. Nano-SiC reinforced Zn biocomposites prepared via laser melting: Microstructure, mechanical properties and biodegradability. J Mater Sci Technol 2019;35:2608–17. https://doi.org/10.1016/j.jmst.2019.06.010.

[15]   Yao X, Moon SK, Lee BY, Bi G. Effects of heat treatment on microstructures and tensile properties of IN718/TiC nanocomposite fabricated by selective laser melting. Int J Precis Eng Manuf 2017;18:1693–1701.

[16]   Gu D, Zhang H, Dai D, Xia M, Hong C, Poprawe R. Laser additive manufacturing of nano-TiC reinforced Ni-based nanocomposites with tailored microstructure and performance. Compos Part B Eng 2019;163:585–97. https://doi.org/10.1016/j.compositesb.2018.12.146.

[17]   Wang P, Zhang B, Tan CC, Raghavan S, Lim YF, Sun CN, et al. Microstructural characteristics and mechanical properties of carbon nanotube reinforced Inconel 625 parts fabricated by selective laser melting. Mater Des 2016;112:290–9. https://doi.org/10.1016/j.matdes.2016.09.080.

[18]   Wang R, Wang W, Zhu G, Pan W, Zhou W, Wang D, et al. Microstructure and mechanical properties of the TiN particles reinforced IN718C composite. J Alloys Compd 2018;762:237–45. https://doi.org/10.1016/j.jallcom.2018.05.096.

[19]   Harrison NJ, Todd I, Mumtaz K. Reduction of micro-cracking in nickel superalloys processed by Selective Laser Melting: A fundamental alloy design approach. Acta Mater 2015;94:59–68. https://doi.org/10.1016/j.actamat.2015.04.035.

[20]   Tomus D, Rometsch PA, Heilmaier M, Wu X. Effect of minor alloying elements on crack-formation characteristics of Hastelloy-X manufactured by selective laser melting. Addit Manuf 2017;16:65–72. https://doi.org/10.1016/j.addma.2017.05.006.

[21]   Marchese G, Basile G, Bassini E, Aversa A, Lombardi M, Ugues D, et al. Study of the microstructure and cracking mechanisms of hastelloy X produced by laser powder bed fusion. Materials (Basel) 2018;11:106. https://doi.org/10.3390/ma11010106.

[22]   Tomus D, Tian Y, Rometsch PA, Heilmaier M, Wu X. Influence of post heat treatments on anisotropy of mechanical behaviour and microstructure of Hastelloy-X

parts produced by selective laser melting. Mater Sci Eng A 2016;667:42–53. https://doi.org/10.1016/j.msea.2016.04.086.

[23] Montero-Sistiaga ML, Pourbabak S, Van Humbeeck J, Schryvers D, Vanmeensel K. Microstructure and mechanical properties of Hastelloy X produced by HP-SLM (high power selective laser melting). Mater Des 2019;105:107598. https://doi.org/10.1016/j.matdes.2019.107598.

[24] Sanchez-Mata O, Wang X, Muñiz-Lerma JA, Shandiz MA, Gauvin R, Brochu M. Fabrication of crack-free nickel-based superalloy considered non-weldable during laser powder bed fusion. Materials (Basel) 2018;11:1288. https://doi.org/10.3390/ma11081288.

[25] Han Q, Gu Y, Setchi R, Lacan F, Johnston R, Evans SL, et al. Additive manufacturing of high-strength crack-free Ni-based Hastelloy X superalloy. Addit Manuf 2019;30:100919. https://doi.org/10.1016/j.addma.2019.100919.

[26] Han Q, Geng Y, Setchi R, Lacan F, Gu D, Evans SL. Macro and nanoscale wear behaviour of Al-Al2O3 nanocomposites fabricated by selective laser melting. Compos Part B Eng 2017;127:26–35. https://doi.org/10.1016/j.compositesb.2017.06.026.

[27] Standard Test Methods for Tension Testing of Metallic Materials n.d. https://compass.astm.org/Standards/HISTORICAL/E8E8M-13A.htm (accessed February 15, 2020).

[28] Han Q, Setchi R, Lacan F, Gu D, Evans SL. Selective laser melting of advanced Al-Al2O3 nanocomposites: Simulation, microstructure and mechanical properties. Mater Sci Eng A 2017;698:162–73. https://doi.org/10.1016/j.msea.2017.05.061.

[29] Han Q, Gu Y, Soe S, Lacan F, Setchi R. Effect of hot cracking on the mechanical properties of Hastelloy X superalloy fabricated by laser powder bed fusion additive manufacturing. Opt Laser Technol 2020;124:105984. https://doi.org/10.1016/j.optlastec.2019.105984.

[30] Scipioni Bertoli U, Wolfer AJ, Matthews MJ, Delplanque JPR, Schoenung JM. On the limitations of Volumetric Energy Density as a design parameter for Selective Laser Melting. Mater Des 2017;113:331–40. https://doi.org/10.1016/j.matdes.2016.10.037.

[31] Iveković A, Omidvari N, Vrancken B, Lietaert K, Thijs L, Vanmeensel K, et al. Selective laser melting of tungsten and tungsten alloys. Int J Refract Met Hard Mater 2018;72:27–32. https://doi.org/10.1016/j.ijrmhm.2017.12.005.

[32] King WE, Barth HD, Castillo VM, Gallegos GF, Gibbs JW, Hahn DE, et al. Observation of keyhole-mode laser melting in laser powder-bed fusion additive manufacturing. J Mater Process Technol 2014;214:2915–25. https://doi.org/10.1016/j.jmatprotec.2014.06.005.

[33] Qi T, Zhu H, Zhang H, Yin J, Ke L, Zeng X. Selective laser melting of Al7050 powder: Melting mode transition and comparison of the characteristics between the keyhole and conduction mode. Mater Des 2017;135:257–66. https://doi.org/10.1016/j.matdes.2017.09.014.

[34] Han Q, Mertens R, Montero-Sistiaga M, Yang S, Setchi R, Vanmeensel K, et al. Laser powder bed fusion of Hastelloy X: effects of hot isostatic pressing and the hot cracking mechanism. Mater Sci Eng A 2018;732:228–39. https://doi.org/https://doi.org/10.1016/j.msea.2018.07.008.

[35] Marchese G, Bassini E, Aversa A, Lombardi M, Ugues D, Fino P, et al. Microstructural evolution of post-processed Hastelloy X alloy fabricated by laser powder bed fusion. Materials (Basel) 2019;12:486. https://doi.org/10.3390/ma12030486.

[36] Zhang Y, Yang L, Dai J, Huang Z, Meng T. Grain growth of Ni-based superalloy IN718 coating fabricated by pulsed laser deposition. Opt Laser Technol 2016;80:220–6. https://doi.org/10.1016/j.optlastec.2016.01.015.

[37] Popovich VA, Borisov E V., Popovich AA, Sufiiarov VS, Masaylo D V., Alzina L. Functionally graded Inconel 718 processed by additive manufacturing: Crystallographic texture, anisotropy of microstructure and mechanical properties. Mater Des 2017;114:441–9. https://doi.org/10.1016/j.matdes.2016.10.075.

[38] Sanaty-Zadeh A. Comparison between current models for the strength of particulate-reinforced metal matrix nanocomposites with emphasis on consideration of Hall-Petch effect. Mater Sci Eng A 2012;531:112–8. https://doi.org/10.1016/j.msea.2011.10.043.

[39] Kang YC, Chan SLI. Tensile properties of nanometric Al2O3 particulate-reinforced aluminum matrix composites. Mater Chem Phys 2004;85:438–43. https://doi.org/10.1016/j.matchemphys.2004.02.002.

[40] Ni X, Kong D, Zhang L, Dong C, Song J, Wu W. Effect of Process Parameters on the Mechanical Properties of Hastelloy X Alloy Fabricated by Selective Laser Melting. J Mater Eng Perform 2019;28:5533–40. https://doi.org/10.1007/s11665-019-04275-w.

[41] Esmaeilizadeh R, Keshavarzkermani A, Ali U, Mahmoodkhani Y, Behravesh B, Jahed H, et al. Customizing mechanical properties of additively manufactured Hastelloy X parts by adjusting laser scanning speed. J Alloys Compd 2020;812:152097. https://doi.org/10.1016/j.jallcom.2019.152097.

[42] Chen JH, Cao R. Micromechanism of Cleavage Fracture of Metals: A Comprehensive Microphysical Model for Cleavage Cracking in Metals. Butterworth-Heinemann; 2014. https://doi.org/10.1016/C2013-0-18727-2.

[43] Ma C, Zhao J, Cao C, Lin TC, Li X. Fundamental study on laser interactions with nanoparticles-reinforced metals-part II: Effect of nanoparticles on surface tension, viscosity, and laser melting. J Manuf Sci Eng Trans ASME 2016;138:121001. https://doi.org/10.1115/1.4033446.

[44] Li XP, Ji G, Chen Z, Addad A, Wu Y, Wang HW, et al. Selective laser melting of nano-TiB2decorated AlSi10Mg alloy with high fracture strength and ductility. Acta Mater 2017;129:183–93. https://doi.org/10.1016/j.actamat.2017.02.062.

[45] Ordonez-Miranda J, Yang R, Alvarado-Gil JJ. Thermal Conductivity of Particulate Nanocomposites. Springer; 2014. https://doi.org/10.1007/978-3-319-02012-9_3.

[46] Tian Z, Hu H, Sun Y. A molecular dynamics study of effective thermal conductivity in nanocomposites. Int J Heat Mass Transf 2013;61:577–82. https://doi.org/10.1016/j.ijheatmasstransfer.2013.02.023.

[47] Ferguson JB, Sheykh-Jaberi F, Kim CS, Rohatgi PK, Cho K. On the strength and strain to failure in particle-reinforced magnesium metal-matrix nanocomposites (Mg MMNCs). Mater Sci Eng A 2012;558:193–204. https://doi.org/10.1016/j.msea.2012.07.111.

[48] Habibnejad-Korayem M, Mahmudi R, Poole WJ. Enhanced properties of Mg-based nano-composites reinforced with Al2O3 nano-particles. Mater Sci Eng A 2009;519:198–203. https://doi.org/10.1016/j.msea.2009.05.001.

[49] Ramakrishnan N. An analytical study on strengthening of particulate reinforced metal matrix composites. Acta Mater 1996;44:69–77. https://doi.org/10.1016/1359-6454(95)00150-9.

[50] Kim CS, Sohn I, Nezafati M, Ferguson JB, Schultz BF, Bajestani-Gohari Z, et al. Prediction models for the yield strength of particle-reinforced unimodal pure magnesium (Mg) metal matrix nanocomposites (MMNCs). J Mater Sci 2013;48:4191–204. https://doi.org/10.1007/s10853-013-7232-x.

[51] Zhou YZ, Volek A. Effect of grain boundary fraction on castability of a directionally solidified nickel alloy. Scr Mater 2006;12:2169–74. https://doi.org/10.1016/j.scriptamat.2006.02.032.